Research Article | Vol. 26, No. 20 | 1 Oct 2018 | OPTICS EXPRESS 25567
Optics EXPRESS

Reconfigurable phase-change meta-absorbers with on-demand quality factor control

SANTIAGO GARCÍA-CUEVAS CARRILLO, ARSENY M. ALEXEEV, YAT-YIN AU AND C. DAVID WRIGHT

College of Engineering, Mathematics and Physical Sciences, University of Exeter, Exeter EX4 4QF, UK
**David.Wright@exeter.ac.uk*

Abstract: Perfect absorber type devices are well-suited to many applications, such as solar cells, spatial light modulators, bio-sensors, and highly-sensitive photo-detectors. In such applications, a method for the design and fabrication of devices in a simple and efficient way, while at the same time maintaining design control over the key performance characteristics of resonant frequency, reflection coefficient at resonance and quality factor, would be particularly advantageous. In this work we develop such a method, based on eigenmode analysis and critical coupling theory, and apply it to the design of reconfigurable phase-change metasurface absorber devices. To validate the method, the design and fabrication of a family of absorbers was carried out with a range of 'on-demand' quality factors, all operating at the same resonant frequency and able to be fabricated simply and simultaneously on the same chip. Furthermore, by switching the phase-change layer between its amorphous and crystalline states, we show that our devices can provide an active or reconfigurable functionality.

Published by The Optical Society under the terms of the Creative Commons Attribution 4.0 License. Further distribution of this work must maintain attribution to the author(s) and the published article's title, journal citation, and DOI.

References

1. K. Yao and Y. Liu, "Plasmonic metamaterials," Nanotechnol. Rev. **3**(2), 177–210 (2014).
2. G. Eleftheriades and M. Selvanayagam, "Transforming electromagnetics using metamaterials," IEEE Microw. Mag. **13**(2), 26–38 (2012).
3. G. Dolling, C. Enkrich, M. Wegener, C. M. Soukoulis, and S. Linden, "Low-loss negative-index metamaterial at telecommunication wavelengths," Opt. Lett. **31**(12), 1800–1802 (2006).
4. H. J. Lezec, J. A. Dionne, and H. A. Atwater, "Negative refraction at visible frequencies," Science **316**(5823), 430–432 (2007).
5. N. Yu and F. Capasso, "Flat optics with designer metasurfaces," Nat. Mater. **13**(2), 139–150 (2014).
6. N. Meinzer, W. L. Barnes, and I. R. Hooper, "Plasmonic meta-atoms and metasurfaces," Nat. Photonics **8**(12), 889–898 (2014).
7. H.-T. Chen, A. J. Taylor, and N. Yu, "A review of metasurfaces: physics and applications," Rep. Prog. Phys. **79**(7), 076401 (2016).
8. N. Yu, P. Genevet, M. A. Kats, F. Aieta, J.-P. Tetienne, F. Capasso, and Z. Gaburro, "Light propagation with phase discontinuities: generalized laws of reflection and refraction," Science **334**(6054), 333–337 (2011).
9. J. P. Balthasar Mueller, N. A. Rubin, R. C. Devlin, B. Groever, and F. Capasso, "Metasurface polarization optics: ndependent phase control of arbitrary orthogonal states of polarization," Phys. Rev. Lett. **118**(11), 113901 (2017).
10. N. I. Landy, S. Sajuyigbe, J. J. Mock, D. R. Smith, and W. J. Padilla, "Perfect metamaterial absorber," Phys. Rev. Lett. **100**(20), 207402 (2008).
11. Y. Cui, Y. He, Y. Jin, F. Ding, L. Yang, Y. Ye, S. Zhong, Y. Lin, and S. He, "Plasmonic and metamaterial structures as electromagnetic absorbers," Laser Photonics Rev. **8**(4), 495–520 (2014).
12. N. I. Zheludev and Y. S. Kivshar, "From metamaterials to metadevices," Nat. Mater. **11**(11), 917–924 (2012).
13. Q. Wang, E. T. F. Rogers, B. Gholipour, C.-M. Wang, G. Yuan, J. Teng, and N. I. Zheludev, "Optically reconfigurable metasurfaces and photonic devices based on phase change materials," Nat. Photonics **10**(1), 60–65 (2016).
14. M. Wuttig, H. Bhaskaran, and T. Taubner, "Phase change materials for non-volatile photonic applications," Nat. Photonics **11**(8), 465–476 (2017).
15. S. Raoux and M. Wuttig, *Phase Change Materials: Science and Applications* (Springer, 2009).
16. B. Gholipour, J. Zhang, K. F. MacDonald, D. W. Hewak, and N. I. Zheludev, "An all-optical, non-volatile, bidirectional, phase-change meta-switch," Adv. Mater. **25**(22), 3050–3054 (2013).

#336466 https://doi.org/10.1364/OE.26.025567
Journal © 2018 Received 29 Jun 2018; revised 30 Aug 2018; accepted 31 Aug 2018; published 17 Sep 2018

Optics EXPRESS

17. K. Shportko, S. Kremers, M. Woda, D. Lencer, J. Robertson, and M. Wuttig, "Resonant bonding in crystalline phase-change materials," Nat. Mater. **7**(8), 653–658 (2008).
18. J.-W. Park, S. H. Eom, H. Lee, J. L. F. Da Silva, Y.-S. Kang, T.-Y. Lee, and Y. H. Khang, "Optical properties of pseudobinary GeTe, $Ge_2Sb_2Te_5$, $GeSb_2Te_4$, $GeSb_4Te_7$, and Sb_2Te_3 from ellipsometry and density functional theory," Phys. Rev. B **80**(11), 115209 (2009).
19. D. Loke, T. H. Lee, W. J. Wang, L. P. Shi, R. Zhao, Y. C. Yeo, T. C. Chong, and S. R. Elliott, "Breaking the speed limits of phase-change memory," Science **336**(6088), 1566–1569 (2012).
20. I. S. Kim, S. L. Cho, D. H. Im, E. H. Cho, D. H. Kim, G. H. Oh, D. H. Ahn, S. O. Park, S. W. Nam, and J. T. Moon, "High performance PRAM cell scalable to sub-20nm technology with below 4F2 cell size, extendable to DRAM applications," in *Symposium on VLSI Technology* (2010), pp. 203–204.
21. P. Hosseini, C. D. Wright, and H. Bhaskaran, "An optoelectronic framework enabled by low-dimensional phase-change films," Nature **511**(7508), 206–211 (2014).
22. X. Yin, T. Steinle, L. Huang, T. Taubner, M. Wuttig, T. Zentgraf, and H. Giessen, "Beam switching and bifocal zoom lensing using active plasmonic metasurfaces," Light Sci. Appl. **6**(7), e17016 (2017).
23. C. Ruiz de Galarreta, A. M. Alexeev, Y.-Y. Au, M. Lopez-Garcia, M. Klemm, M. Cryan, J. Bertolotti, and C. D. Wright, "Nonvolatile peconfigurable phase-change metadevices for beam steering in the near infrared," Adv. Funct. Mater. **28**(10), 1704993 (2018).
24. Y. Chen, X. Li, Y. Sonnefraud, A. I. Fernández-Domínguez, X. Luo, M. Hong, and S. A. Maier, "Engineering the phase front of light with phase-change material based planar lenses," Sci. Rep. **5**(1), 8660 (2015).
25. C. Rios, P. Hosseini, C. D. Wright, H. Bhaskaran, and W. H. P. Pernice, "On-chip photonic memory elements employing phase-change materials," Adv. Mater. **26**(9), 1372–1377 (2014).
26. J. Feldmann, M. Stegmaier, N. Gruhler, C. Ríos, H. Bhaskaran, C. D. Wright, and W. H. P. Pernice, "Calculating with light using a chip-scale all-optical abacus," Nat. Commun. **8**(1), 1256 (2017).
27. Z. Cheng, C. Ríos, W. H. P. Pernice, C. D. Wright, and H. Bhaskaran, "On-chip photonic synapse," Sci. Adv. **3**(9), e1700160 (2017).
28. A. Tittl, A.-K. U. Michel, M. Schäferling, X. Yin, B. Gholipour, L. Cui, M. Wuttig, T. Taubner, F. Neubrech, and H. Giessen, "A switchable mid-infrared plasmonic perfect absorber with multispectral thermal imaging capability," Adv. Mater. **27**(31), 4597–4603 (2015).
29. Z. Zhu, P. G. Evans, R. F. Haglund, Jr., and J. G. Valentine, "Dynamically reconfigurable metadevice employing nanostructured phase-change materials," Nano Lett. **17**(8), 4881–4885 (2017).
30. T. G. Mayerhofer, R. Knipper, U. Hübner, D. Cialla-May, K. Weber, H.-G. Meyer, and J. Popp, "Ultra sensing by combining extraordinary optical transmission with perfect absorption," ACS Photonics **2**(11), 1567–1575 (2015).
31. S. G. Carrillo, G. R. Nash, H. Hayat, M. J. Cryan, M. Klemm, H. Bhaskaran, and C. D. Wright, "Design of practicable phase-change metadevices for near-infrared absorber and modulator applications," Opt. Express **24**(12), 13563–13573 (2016).
32. T. Cao, C. W. Wei, R. E. Simpson, L. Zhang, and M. J. Cryan, "Broadband polarization-independent perfect absorber using a phase-change metamaterial at visible frequencies," Sci. Rep. **4**(1), 3955 (2014).
33. T. Maier and H. Brueckl, "Multispectral microbolometers for the midinfrared," Opt. Lett. **35**(22), 3766–3768 (2010).
34. F. B. P. Niesler, J. K. Gansel, S. Fischbach, and M. Wegener, "Metamaterial metal-based bolometers," Appl. Phys. Lett. **100**(20), 203508 (2012).
35. C. Wu, B. Neuner III, J. John, A. Milder, B. Zollars, S. Savoy, and G. Shvets, "Metamaterial-based integrated plasmonic absorber/emitter for solar thermo-photovoltaic systems," J. Opt. **14**(2), 024005 (2012).
36. S. Ogawa and M. Kimata, "Wavelength-or polarization-selective thermal infrared detectors for multi-color or polarimetric imaging using plasmonics and metamaterials," Materials (Basel) **10**(5), 493 (2017).
37. K. Fan, J. Y. Suen, and W. J. Padilla, "Graphene metamaterial spatial light modulator for infrared single pixel imaging," Opt. Express **25**(21), 25318–25325 (2017).
38. K. Chen, R. Adato, and H. Altug, "Dual-band perfect absorber for multispectral plasmon-enhanced infrared spectroscopy," ACS Nano **6**(9), 7998–8006 (2012).
39. C. Huck, J. Vogt, M. Sendner, D. Hengstler, F. Neubrech, and A. Pucci, "Plasmonic enhancement of infrared vibrational signals: nanoslits versus nanorods," ACS Photonics **2**(10), 1489–1497 (2015).
40. T. G. Mayerhöfer and J. Popp, "Periodic array-based substrates for surface-enhanced infrared spectroscopy," Nanophotonics **7**(1), 39–79 (2018).
41. T. Cao, C. Wei, R. E. Simpson, L. Zhang, and M. J. Cryan, "Rapid phase transition of a phase-change metamaterial perfect absorber," Opt. Mater. Express **3**(8), 1101–1110 (2013).
42. P. Zhu and L. Jay Guo, "High performance broadband absorber in the visible band by engineered dispersion and geometry of a metal-dielectric-metal stack," Appl. Phys. Lett. **101**(24), 241116 (2012).
43. A. Tittl, M. G. Harats, R. Walter, X. Yin, M. Schäferling, N. Liu, R. Rapaport, and H. Giessen, "Quantitative angle-resolved small-spot reflectance measurements on plasmonic perfect absorbers: impedance matching and disorder effects," ACS Nano **8**(10), 10885–10892 (2014).
44. J. Hao, L. Zhou, and M. Qiu, "Nearly total absorption of light and heat generation by plasmonic metamaterials," Phys. Rev. B **83**(16), 165107 (2011).
45. R. Alaee, M. Albooyeh, S. Tretyakov, and C. Rockstuhl, "Phase-change material-based nanoantennas with tunable radiation patterns," Opt. Lett. **41**(17), 4099–4102 (2016).

Optics EXPRESS

46. C. Wu, B. Neuner, G. Shvets, J. John, A. Milder, B. Zollars, and S. Savoy, "Large-area wide-angle spectrally selective plasmonic absorber," Phys. Rev. B **84**(7), 075102 (2011).
47. C. Qu, S. Ma, J. Hao, M. Qiu, X. Li, S. Xiao, Z. Miao, N. Dai, Q. He, S. Sun, and L. Zhou, "Tailor the functionalities of metasurfaces based on a complete phase diagram," Phys. Rev. Lett. **115**(23), 235503 (2015).
48. S. D. Rezaei, J. Ho, R. J. H. Ng, S. Ramakrishna, and J. K. W. Yang, "On the correlation of absorption cross-section with plasmonic color generation," Opt. Express **25**(22), 27652–27664 (2017).
49. H. a Haus, "Waves and Fields in Optoelectronics," (1984).
50. Y.-Y. Au, H. Bhaskaran, and C. D. Wright, "Phase-change devices for simultaneous optical-electrical applications," Sci. Rep. **7**(1), 9688 (2017).
51. A. Pors and S. I. Bozhevolnyi, "Plasmonic metasurfaces for efficient phase control in reflection," Opt. Express **21**(22), 27438–27451 (2013).
52. T. Søndergaard, J. Jung, S. I. Bozhevolnyi, and G. Della Valle, "Theoretical analysis of gold nano-strip gap plasmon resonators," New J. Phys. **10**(10), 105008 (2008).
53. Q. Bai, M. Perrin, C. Sauvan, J.-P. Hugonin, and P. Lalanne, "Efficient and intuitive method for the analysis of light scattering by a resonant nanostructure," Opt. Express **21**(22), 27371–27382 (2013).
54. R. Horst, P. M. Pardalos, and N. Van Thoai, *Introduction to Global Optimization* (Springer Science & Business Media, 2000).
55. R. Horst and H. Tuy, *Global Optimization: Deterministic Approaches* (Springer Science & Business Media, 2013).
56. Y.-C. Chung, P.-J. Cheng, Y.-H. Chou, B.-T. Chou, K.-B. Hong, J.-H. Shih, S.-D. Lin, T.-C. Lu, and T.-R. Lin, "Surface roughness effects on aluminium-based ultraviolet plasmonic nanolasers," Sci. Rep. **7**(1), 39813 (2017).
57. A. D. Rakic, A. B. Djurišic, J. M. Elazar, and M. L. Majewski, "Optical properties of metallic films for vertical-cavity optoelectronic devices," Appl. Opt. **37**(22), 5271–5283 (1998).

1. Introduction

The ability to design devices capable of controlling the propagative characteristics of light in the infrared part of the electromagnetic spectrum is essential to a number of technologically important fields, such as telecommunications, sensing, imaging, spectroscopy, security and bio-sensing. In recent decades, the progress in these fields has been substantially influenced by the rise of plasmonic metamaterials. Plasmonic metamaterials [1,2] are artificial structures composed of metallic nanoresonators arranged in periodic sub-wavelength arrays. The resonators can be designed to have effective permittivities and permeabilities not achievable using conventional materials [3,4]. Plasmonic metasurfaces [5–7], two-dimensional counterparts of plasmonic metamaterials, are particularly interesting from the practical point of view, as their fabrication is fairly straightforward and they can offer relatively small insertion losses. Different kinds of plasmonic metasurfaces have been proposed in the literature to serve a wide range of applications, such as beam steering [8], polarization control [9] and perfect absorption [10,11]. Furthermore, to achieve dynamic tunability and/or reconfigurability, so creating active devices, plasmonic metasurfaces can also be combined with liquid crystals, gated semiconductors, or, as in this work, phase-change materials [12,13].

The phase-change material (PCM) based approach stands out from the other means of creating dynamic and reconfigurable plasmonic metasurfaces [14]. PCMs typically comprise thin-films of chalcogenide alloys, such as the well-known ternary material $Ge_2Sb_2Te_5$. Under electrical, optical or thermal stimulus, PCMs undergo a phase transition, i.e. switch between amorphous and crystalline states, with a resulting dramatic change in their electrical and optical properties [15]. Amorphization requires temperatures in the phase-change material to reach melting point (~900 K for $Ge_2Sb_2Te_5$) and be followed by a very fast cooling (tens of degrees per nanosecond for $Ge_2Sb_2Te_5$) [15]. Crystallization requires lower temperatures, lying between the glass-transition and melting temperatures [15]. PCMs possess a high optical contrast (refractive index difference) between phase states in the infrared region and nearly-zero optical losses when in the amorphous state [16–18]. They also benefit from fast switching (sub-nanosecond electrically [19] and tens of picoseconds optically [14]), high endurance (potentially up to 10^{15} switching cycles [20]) and, importantly, they exhibit non-volatility in both phases (and even in mixed, i.e. fractionally-crystallized, phases). This allows for the utilization of chalcogenide PCMs in a variety of novel and reconfigurable infra-red devices such as non-volatile solid-state reflective displays [21], optical beam steerers [22,23], spatial light modulators [12], reconfigurable lenses [13,24], integrated photonic memories and

Optics EXPRESS

computing devices [25–27] and, the topic of this paper, PCM-based reconfigurable perfect absorbers [28–32].

Perfect absorbers can be utilized in a number of infrared device applications, for instance, radiation detectors [28,33,34], solar cells [35], spatial light modulators [29,36,37] and bio-sensing [30,38–40]. Various approaches have been used in the literature to design and explain the operation of perfect metamaterial absorbers, including analogies with plasmon slot waveguides [41,42], optical impedance matching [43,44], application of the first Kerker condition [45], critical coupling mechanisms [46,47] and considerations of the absorption cross section of the resonators that comprise the metasurfaces [48]. All of these methods succeed in giving an explanation of the operation of perfect absorbers, however they differ significantly in terms of complexity and, importantly, their ability for quantitative design of the device response. Indeed, since the performance of metamaterial perfect absorbers can be broadly described by a few key parameters, namely the resonant frequency, bandwidth, quality factor and reflection coefficient (at resonance), a quantitative design methodology that predicts performance in these terms, in a simple and economical manner, is vital when trying to engineer device specifications that a certain application demands. For instance, in the field of infrared spectroscopy, perfect absorbers have been used to enhance the interaction of infrared radiation with biological analytes [30,38,39]. Here, by controlling the quality factor of the device, one can achieve a better analyte selectivity. Moreover, for increased sensitivity of detection, accurate control of the absorber's coupling to the incoming radiation is crucial [40]. To give another example, in the field of plasmonic color printing, figures of merit such as the color saturation are directly related to the quality factor of the resonant absorption spectra [48]. Finally, as a last example of the importance of a quantitative methodology for designing the quality factor in optical devices, we note that in metal-insulator-metal structures used to create (optical) phase gradient metasurfaces with beam steering capabilities [23], control of the quality factor is important since it determines how sharply the optical phase varies around resonance. (We also note that the requirement of a full 2π phase coverage is present only in overcoupled resonators) [47,49].

In this paper, therefore, we derive, based on eigenmode calculations together with the concept of critical coupling [46], a design methodology that is not only relatively simple but which is also inherently well-suited to the quantitative design/selection of key absorber parameters including the resonant frequency, bandwidth and degree of coupling (minimum reflection at resonance). Moreover, we demonstrate the validity of our proposed methodology via the experimental fabrication and characterization of PCM-based reconfigurable absorbers working in the near infrared waveband ($\lambda = 1550$ nm) and with a purposely engineered quality factor. Our devices are made with a nanostrip Al metasurface placed on top of a layered structure comprising a thin ITO film, a chalcogenide phase-change material $Ge_2Sb_2Te_5$ (GST) and a bottom Al mirror (see Fig. 1) [31]. The ITO is used to prevent environmental oxidation of the GST layer, while it can be also utilized as a top electrode for electrical switching of the GST [21,50]. By transforming the GST between the amorphous and crystalline states our device can be operated in two distinctly different regimes. When the GST is in the amorphous state, the resonant gap plasmon [51,52] of the metal-dielectric-metal structure is excited and the incoming radiation is absorbed (with the amount of absorption dependent on the degree of coupling). However, when GST layer is switched into the crystalline state the resonance condition is lifted due to the change of the refractive index, resulting in specular reflection of the incoming radiation.

We show how the absorber resonant frequency can be accurately calculated for a structure composed of materials that presents optical losses, using the result to obtain external and internal decay rates of the device [53]. These decay rates define two most important parameters of a practical absorber - i.e. the quality factor and the reflection coefficient at resonance [49]. It is shown that the quality factor of our devices can be controlled, for a fixed operating frequency, by changing only one design parameter - the periodicity of the nanostrips

Optics EXPRESS

comprising the optical metasurface - while leaving other design parameters intact. This allows us to produce simple guidelines for engineering absorbers with desired characteristics, without the need to run time-consuming finite element (FEM) simulations. We test the practicability of our modeling results by fabricating several representative devices and measuring their amorphous and crystalline responses.

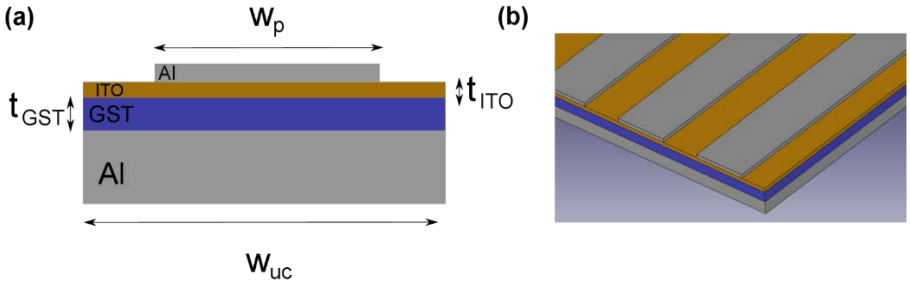

Fig. 1. (a) 2D cross section of the unit cell of the reconfigurable phase-change absorber device. Dimensions that define the optical response of the device are shown, as well as the different material layers used. (b) 3D schematic of (part of) the device.

2. Results and Discussion

2.1 Quality factor engineering

Eigenmode calculations were used to optimize a number of device geometrical parameters so that phase-change absorbers, of the type shown in Fig. 1, could be realized with various quality factors at the resonant wavelength of $\lambda = 1550$ nm. More specifically, the following device parameters - nanostrip resonator width, w_p, thickness of the GST layer, t_{gst}, and metasurface period, w_{uc}, - were swept using an optimization routine to achieve the required optical performance. We employed a numerical technique developed by Bai *et. al*. to excite the structure with a complex eigenfrequency [53]. In essence, the method allows us to design a structure with a desired quality factor using the following steps: (i) Excite the device structure with a complex frequency, $\omega + i/\tau$, where $1/\tau$ is the decay rate associated with the amplitude of the oscillation for the loaded resonator (called total decay rate in the rest of the manuscript). The real part of the excitation frequency ω is fixed while the imaginary part $1/\tau$ is varied in each simulation to achieve devices with desired quality factors. (ii) Search for a device geometry (i.e., in our case, search for values of layer thicknesses, metasurface strip widths and periodicity) that makes the modulus of the electric field evaluated close to the resonator to diverge when excited with the chosen complex (resonance) frequency. This search is done using a global optimization algorithm [54,55]. (iii) Once the optimal structure is found, we can relate the value of τ to the value of the quality factor as $Q = \omega_0\tau/2$ [49]. This means that in Step 1 we have chosen the desired quality factor of the structure, provided that we can find an appropriate device geometry in Step 2 (see Methods for further details). This results in significant gains in computational efficiency in the design of devices (as compared to conventional FEM simulations) since we essentially 'tell' the model at which frequency the resonance is required using the real part of the desired eigenfrequency, and we will introduce information about the bandwidth (quality factor) in the imaginary part of the eigenfrequency. So, we are able to directly target the resonant position and bandwidth of the device with far fewer calculations than in the case of a conventional design approach.

Ten different absorber device designs (each design being a vector in the parametric space w_{uc}, w_p and t_{gst}) were obtained for values of the quality factor $Q = 4, 4.5, 5, 5.5, 6$. In Fig. 2(a), the resulting width of the nanostrip resonators w_p is plotted versus the thickness of the GST layer t_{gst} for all cases. It can be seen that all curves cross in a very small region of the graph. This implies that for fixed values of w_p and t_{gst} (the crossing point in the plot) one can obtain any desired value of Q (within the range examined here) by varying only the width of the unit

Optics EXPRESS

cell w_{uc}. To verify this, another set of simulations was carried out to again find structures with Q = 4, 4.5, 5, 5.5, 6, but this time we restricted the values of w_p and t_{gst} to be within the narrow region where all the curves in Fig. 2(a) cross (more specifically, for convergence purposes, we set this region to be 2 nm wide in the w_p direction and 1 nm wide in the t_{gst} direction). The results are shown in Fig. 2(b) and confirm that we can link the quality factor of our devices to only one geometrical parameter, namely the periodicity of the top plasmonic metasurface, w_{uc}. This is a key finding of the current work, showing how a "family" of absorbers having the same resonant frequency but different Q factors can be readily designed, and subsequently fabricated, using essentially the same device structure (apart from the value of w_{uc}).

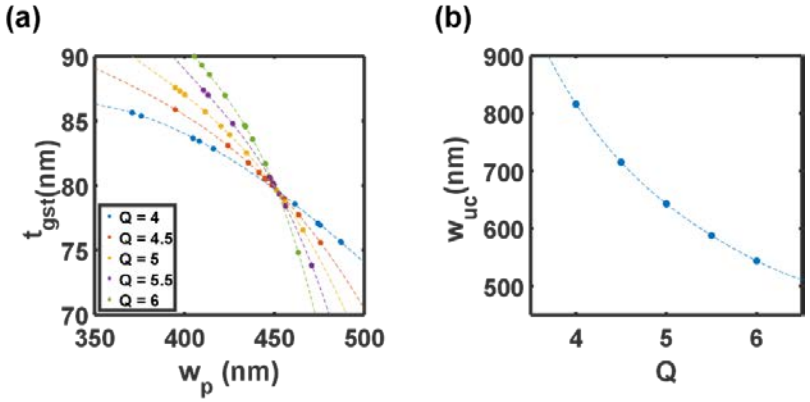

Fig. 2. (a) Perfect phase-change absorbers of various geometries optimized to possess desired quality factors (each color indicates devices with equal values of Q). (b) Width of the unit cell w_{uc} against the corresponding value of Q (the data in this plot corresponds to the optimized devices in the region where curves cross in (a)). Dashed lines are guides for the eye only.

2.2 Reflectance Calculations

Having designed, using the eigenmode approach described above, phase-change absorbers resonant at 1550 nm and with a range of quality factors, we next, using 'conventional' FEM techniques [31] (see Methods section), simulated their reflectance spectra over the wavelength range from 1000 to 1600 nm (note that 1600 nm is the longest wavelength examined since this corresponds to the maximum operating wavelength of our spectrophotometer – see Methods section). This enables us to observe the change in the bandwidth and in the reflection coefficient at resonance for different quality factors. Thus, in Fig. 3(a)-(c) we plot simulated reflectance spectra for devices with Q = 4.5 (w_{uc} = 715 nm), Q = 5 (w_{uc} = 643 nm), and Q = 5.5 (w_{uc} = 588 nm).

We also fabricated devices having the same (nominal) nanostrip periodicities, w_{uc}, as those in Fig. 3(a)-(c), and measured their experimental reflectance spectra. The results are shown in Fig. 3(d)-(f) (insets show SEM images of the fabricated devices). There is very good agreement between the modeling and experimental results (note that the width of the nanostrip resonators, w_p, hardly deviates from the target value of 451 nm for any of the devices, as can be seen from the Appendix at the end of this manuscript).

Finally, we show experimentally the reconfigurability of our phase-change absorbers by switching the GST layer from the amorphous to crystalline state, here using controllable thermal heating on the hot plate. As discussed in the introduction, after switching, the resonant condition of the device is lifted, resulting in mirror-like specular reflection with efficiency here of above 60% (see Figs. 3(d)-3(f)). Therefore, our devices are indeed reconfigurable and could be used, for example as light modulator here working in reflection and at 1550 nm wavelength (to the best of our knowledge, this is the first experimental demonstration of GST-based reconfigurable perfect absorbers operating in the near-IR band) (See Appendix at the end of this manuscript for details on practical approaches to the switching of devices).

Optics EXPRESS

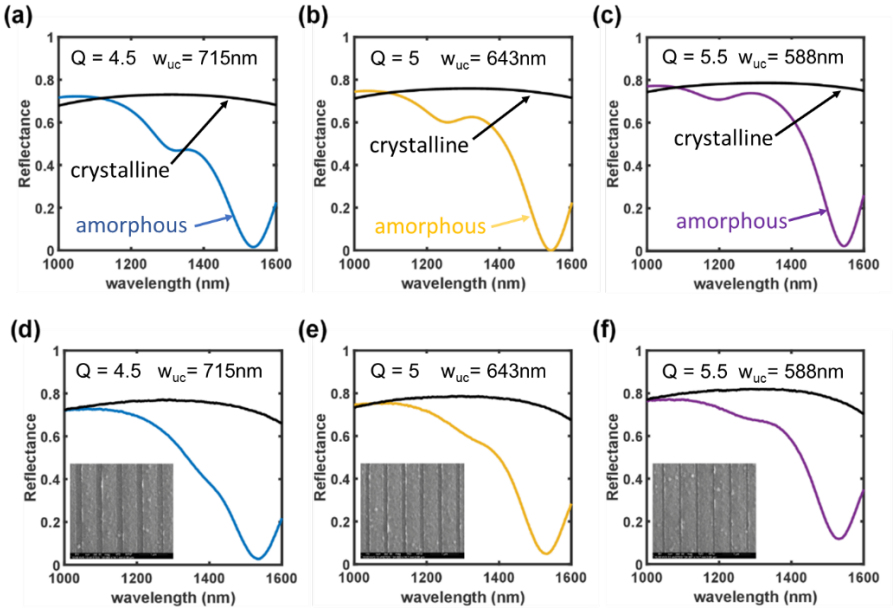

Fig. 3. (a), (b), (c) Simulated reflectance spectra for designs with fixed values of w_p and t_{gst} and with Q = 4.5, 5, 5.5 respectively and with the GST layer in the amorphous (colored lines) and crystalline (black lines) states. (d), (e), (f) Experimental reflectance spectra for fabricated devices with the same designs as in top panels (and again with the GST in amorphous and crystalline phases). Insets in (d) to (f) show SEM images of the fabricated devices.

2.3 Critically coupled absorbers

The eigenmode and reflectance calculations presented in the previous section allow for accurate extraction of the external and internal decay rates - important characteristics of a practical perfect absorber. The quality factor of a resonating structure, such as perfect absorber, can be expressed through its total decay rate as $Q = \omega_0\tau/2$, where ω_0 is the resonance frequency and $1/\tau$ is the total decay rate. In turn, the total decay rate $1/\tau$ is defined by the internal and external decay rates of the structure, according to the relation:

$$\frac{1}{\tau} = \frac{1}{\tau_0} + \frac{1}{\tau_e} \tag{1}$$

Here $1/\tau_0$ is the internal decay rate, i.e. the time measure of the internal losses of the resonator through electron scattering, and $1/\tau_e$ is the external decay rate, i.e. the time measure of the external losses of the resonator through the emission of radiation. The reflection coefficient $\Gamma(\omega)$ can be expressed in terms of the decay rates as [49]:

$$\Gamma(\omega) = \frac{1/\tau_e - 1/\tau_0 - i(\omega - \omega_0)}{1/\tau_e + 1/\tau_0 + i(\omega - \omega_0)} \tag{2}$$

Thus, once the resonant frequency has been identified via eigenmode calculations, and the reflectance coefficient at resonance evaluated (via FEM simulations of the type used to generate Fig. 3(a)-(c), but carried out only at ω_0), then Eq. (1) and (2) can be solved simultaneously to obtain the values of $1/\tau_0$ and $1/\tau_e$ at ω_0.

The decay rates thus calculated for a set of perfect absorbers with fixed values of t_{gst} and w_p but with differing values of Q are plotted in Fig. 4(a). The interplay between internal and external decay rates determines the onset of critical coupling of the absorber to the incident radiation [47]. As is well known, the device is critically coupled when $1/\tau_0 = 1/\tau_e$ and in such a

Optics EXPRESS

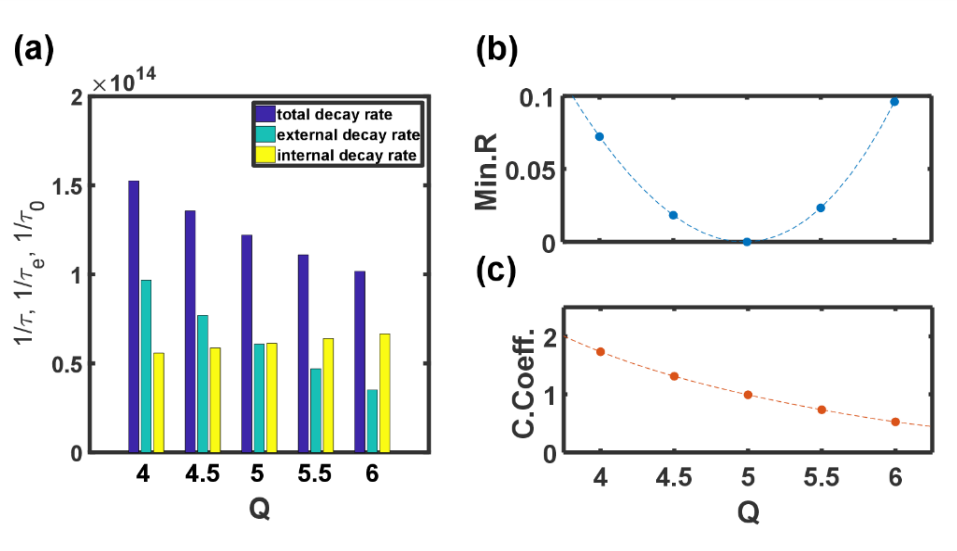

Fig. 4. (a) Total, internal, and external decay rates as a function of *Q*. (b) Minimum reflectance and (c) coupling coefficient as a function of *Q*. Dashed lines in (b) and (c) are guides for the eye only.

case all the incoming radiation is perfectly absorbed at resonance. This condition implies matching of the free space impedance to the impedance of the resonating structure. It can also be interpreted as the when the absorption cross section is equal to the unit cell area [48]. According to the results shown in Fig. 4(a), critical coupling should occur in our devices when $Q = 5$ (when $w_{uc} = 643$ nm). This is confirmed in Fig. 4(b), where the reflectance at resonance is shown for all *Q* values examined here; the reflectance is zero (perfect absorption) only for the case when $Q = 5$. Thus, although we can easily obtain (design) absorbers with a range of *Q* factors, this comes at a price of higher reflection at resonance (but the reflectance is still below 10% at resonance for all the devices studied here).

It is also convenient to introduce another measure of the performance of the perfect absorber, namely the coupling coefficient $CC = \tau_0/\tau_e$, which is plotted in Fig. 4(c). Absorbers with $CC > 1$ ($\tau_0 > \tau_e$) are overcoupled, those with $CC > 1$ ($\tau_0 < \tau_e$) are undercoupled, while those with $CC = 1$ are critically coupled. The results of Fig. 4(c) also demonstrate a clear correspondence between the degree of coupling and the quality factor, reiterating the point that it is not possible to design-in an arbitrary value of *Q* for any given degree of coupling (for fixed t_{gst} and w_p values, as used here).

It is also convenient to introduce another measure of the performance of the perfect absorber, namely the coupling coefficient $CC = \tau_0/\tau_e$, which is plotted in Fig. 4(c). Absorbers with $CC > 1$ ($\tau_0 > \tau_e$) are overcoupled, those with $CC > 1$ ($\tau_0 < \tau_e$) are undercoupled, while those with $CC = 1$ are critically coupled. The results of Fig. 4(c) also demonstrate a clear correspondence between the degree of coupling and the quality factor, reiterating the point that it is not possible to design-in an arbitrary value of *Q* for any given degree of coupling (for fixed t_{gst} and w_p values, as used here).

To explore in a little more detail the occurrence of critical coupling in our phase-change absorbers, we compare in Fig. 5 FEM simulated and experimentally measured reflectance spectra for five sets of devices, having nanostrip periodicities ranging from 544 to 816 nm. There is generally good agreement between the simulated (Fig. 5(a)) and experimental (Fig. 5(b)) results, apart from a mismatch in the minimum reflectance values.

Optics EXPRESS

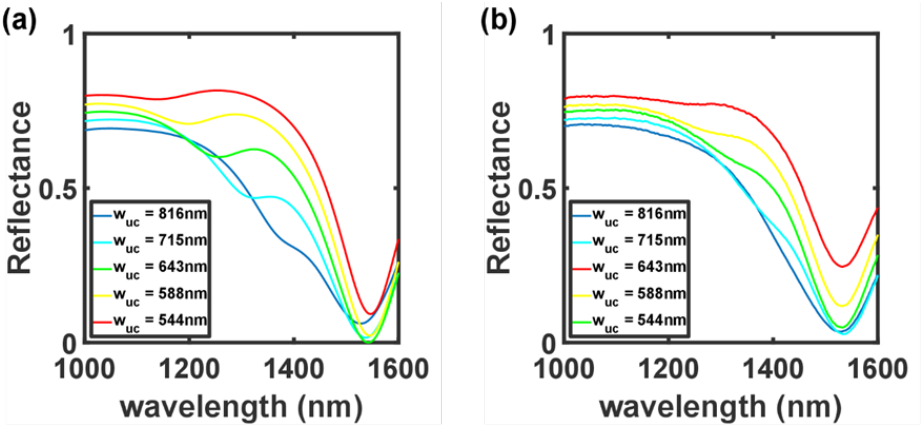

Fig. 5. (a) Modelled reflectance spectra for a family of phase-change absorbers (GST layer in the amorphous state) obtained by varying only the periodicity of the metasurface (the Al nanostrips). (b) Experimental reflectance spectra for fabricated devices having the same geometries as in (a).

In particular, we note that, according to the simulations, the absorber with a nanostrip periodicity of 643 nm (w_{uc} = 643 nm) should be the one which is critically coupled, while in the experimental results it is the device with w_{uc} = 715 nm which is closest to being critical coupled. This discrepancy can be explained by an internal decay rate that is larger in the fabricated devices as compared to that in the simulations. This most likely arises due to fabrication imperfections, in particular a non-negligible roughness of the surface of the Al film used to make the periodic nanostrips. The roughness of Al films is known to increase electronic scattering, so affecting their effective optical properties (n and k) and increasing losses and decreasing the quality factor [56]. Indeed, from Fig. 4(a) it can be seen that if the internal losses were increased slightly (increased internal decay rate) then the absorber with Q = 4.5 (w_{uc} = 715 nm) would be (closest to being) at the critical coupling condition, while devices with higher Q values (w_{uc} < 715 nm) would possess a monotonically increasing reflectance at resonance. This is precisely the behavior seen in the experimental results of Fig. 5(b). Thus, although the underestimation of the internal losses of our devices resulted in the mismatch between simulated and measured values of the minimum absorber reflectance, this does not affect general findings of the current work.

2.4 "On-Demand" quality factors

The above findings clearly show that by fixing two main design parameters of the proposed perfect absorbers – the GST layer thickness, t_{gst}, and width of the plasmonic strip resonators, w_p, - it is possible to control the quality factor and coupling coefficient of the device by changing only the resonator periodicity, w_{uc}. Thus, once optimal values of t_{gst} and w_p are found, the need to run conventional FEM simulations (that can be both time and computer power consuming) can be avoided. In fact, as we show below, we can go further and produce simple guidelines that allow the design of perfect absorbers with specific 'on-demand' Q factors.

These simple guidelines are summarized and tested in Fig. 6. The internal decay rate $1/\tau_0$ is observed to vary approximately linearly with the inverse of the width of the unit cell, w_{uc}, as shown in Fig. 6(a). In contrast, the external decay rate, $1/\tau_e$, increases linearly with w_{uc}, as can be seen from Fig. 6(b). Therefore, using Eq. (1) and (2), we can obtain a simple and quick way to calculate the Q value, for a given value of w_{uc}, via the relationship:

$$\frac{1}{Q} = \frac{2}{\omega_0}\left(\frac{1}{\tau_0} + \frac{1}{\tau_e}\right) \tag{3}$$

Optics EXPRESS

with $1/\tau_0 = k_0 / w_{uc} + C_0$ where k_0 (= 1.761x10^{16} nm^{-1}s^{-1}) and C_0 (= 3.409x10^{13} s^{-1}) are the regression coefficients of the linear fitting in Fig. 6(a), and $1/\tau_e = k_e w_{uc} + C_e$ where k_e (= 2.261x10^{11} nm^{-1}s^{-1}) and C_e (= –8.612x10^{13} s^{-1}) are the regression coefficients of the linear fitting shown in Fig. 6(b).

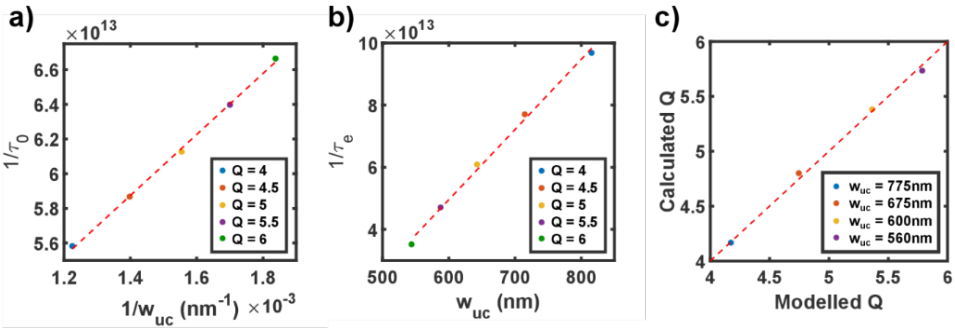

Fig. 6. (a) Internal decay rate as a function of the inverse of the plasmonic metasurface periodicity w_{uc} (dashed line is a linear best-fit). (b) External decay rate as a function of the inverse of the plasmonic metasurface periodicity w_{uc} (dashed line is a linear best-fit). c) Calculated values of Q using the data in (a) and (b) against the values for Q obtained from FEM modeling for the same structures (the dashed "45° line" is shown for visual guidance only).

The results of applying Eq. (3) to find Q for the cases with w_{uc} = 560, 600, 675, 775 nm are shown in Fig. 6(c), where they are compared to Q values calculated via eigenmode simulations. It is clear that that there is excellent agreement between both techniques. Thus, using eigenmode calculations and critical coupling concepts, we have shown that it is possible to design perfect absorbers having a particular desired quality factor (at least over the range of Q values studied here, see the appendix for a discussion on what affects the range of Q values achievable), simply by changing the periodicity of the top plasmonic metasurface.

3. Conclusions

In conclusion, we have presented a design method to control the main aspects that define the performance of perfect absorbers, i.e., the resonant frequency, bandwidth and reflection coefficient at resonance. To validate the method, we designed and fabricated a family of reconfigurable phase-change perfect absorbers having desired quality factors, obtaining very good agreement between theory and experiment. Moreover, analysis based on a critical coupling approach allowed us to establish simple relationships between device geometry and performance. In particular, we showed how the width of the unit cell is (for fixed values of other device geometric parameters) linked directly to the value of Q. As a result, we could greatly simplify the design and fabrication process of the absorber devices. We demonstrated this by producing a family of devices with a range of 'on-demand' quality factors, all operating at the same resonant frequency and able to be fabricated simultaneously on the same chip (i.e., all with the same layer thicknesses and all with the same width of the top optical metasurface nanostrips). Furthermore, by switching the phase-change (GST) layer in the absorber structure between its amorphous and crystalline states, we showed that our devices can be switched on and off, thus allowing for the design of active and reconfigurable components. For example, we might imagine an application where, by monitoring the interaction of incident radiation with a series of selectively enabled phase-change absorber devices having various quality factors, one can estimate in a quick and simple way the bandwidth of the signal under detection. More generally, our design approach is likely to find use wherever precise control over the resonant frequency and quality factor of plasmonic metasurface resonant absorbers type structures is desired.

Optics EXPRESS

4. Methods

Numerical Simulations: COMSOL Multiphysics finite-element modeling in the 2D frequency-domain was used to obtain eigenmodes (as described below) and reflectance spectra (as described in [31]) of the system. A square unit cell which contained single plasmonic nanostrip resonator was studied (see Fig. 1). Bloch-Floquet periodic conditions were applied to both sides of the unit cell in order to simulate an infinite array. Perfectly matched layers were placed as the top and bottom boundaries of the unit cell. Ports were placed above and below the structure to study reflection of the structure excited with plane waves of a chosen frequency. Optical properties of all materials constituting the device used in the simulations can be found in the Appendix at the end of this manuscript.

Eigenmode Calculations: As pointed out by Bai et al. [53], it is possible to calculate the complex eigenfrequency of a resonant nanostructure (such those examined here) in the presence of losses by searching for the complex frequency that makes the near-field diverge. Alternatively, one can search for a structure geometry that makes the electric field diverge at a specific complex frequency. We adopted this latter approach, since it allowed the design of structures that resonate at a particular chosen (designed-in) frequency and which possess a given quality factor (since the complex eigenfrequency $\omega_0 + i/\tau$ of a resonating structure is related with the quality factor as $Q = \omega_0\tau/2$) [49]. Thus, we used a numerical implementation (carried out in COMSOL Multiphysics) as described by Bai et. al. [53] for our eigenmode calculations, coupling this to optimization routines, built into the Global Optimisation Toolbox of Matlab, to search for the device geometries (values of w_{uc}, w_p and t_{gst} in our case) required to deliver the desired quality factors.

Fabrication of devices: Magnetron sputtering was used to deposit the stack of layers - Al/GST/ITO - on top of a silicon substrate, and then to deposit the top array of Al plasmonic resonators. Deposition of the Al/GST/ITO stack was done in a single run without breaking the vacuum. The following sputtering conditions were used: Ar pressure - 1 × 10–3 Torr; magnetron power for Al deposition - 170 W (DC); magnetron power for GST and ITO depositions - 25 W (DC). E-beam lithography was employed to create the Al plasmonic resonators. First, PMMA 950K A4 was spun on top of the Al/GST/ITO stack at 4000 rpm to obtain a 200 nm resist film. Baking of the PMMA film was done at 100°C on a hot plate for 10 minutes (a low baking temperature was deliberately chosen to avoid crystallization of the GST layer, which is amorphous in the as-deposited state). The following conditions were used during e-beam exposure: accelerating voltage - 80 kV, gun current – 1.5 nA, exposure dose 7.4 C m-2. After exposure the PMMA film was developed in IPA:MIBK:MEK 15:5:1 solution for 35 seconds at room temperature. Finally, Al was deposited into the created PMMA mask as described above. Lift-off of the de-posited Al film was achieved by placing the sample in ace-tone at 60°C for 2 hours with mild sonication at 80 kHz. Crystallization of the GST layer (for demonstration of the reconfigurability of the devices) was achieved by placing samples on a hot plate at 250°C for 15 mins.

Optical Measurements: Optical measurements of the reflectance spectra of devices were carried out using a Jasco MSV-5300 UV-Visible/NIR Microspectrometer. The aperture selected for the measurement was 15 μm in diameter. The polarizer in the microspectrometer was oriented perpendicularly to the orientation of the top Al strips. A calibrated aluminum mirror was used to normalize (calibrate) the reflectance measurements.

Appendix

The quality factor

In a resonator, the relationship of the dissipated power P and the energy of the system U is approximately linear, i.e.:

Optics EXPRESS

$$P = -\frac{dU}{dt} = \alpha U \tag{4}$$

The rate of energy dissipation in the resonator is proportional to the amount of the stored energy. Solving the above equation we obtain

$$U = U_0 e^{-\alpha t} \tag{5}$$

and by combining both these equations together we get

$$P = \alpha U_0 e^{-\alpha t} = P_0 e^{-t/\tau_{eng}} \tag{6}$$

where $\alpha = 1/\tau_{eng}$ with τ_{eng} being the time constant for the energy decay. The quality factor is defined as $Q = \omega_0 \tau_{eng}$. It thus follows that

$$P = \frac{U}{\tau_{eng}} = \frac{\omega_0 U}{Q} \tag{7}$$

The time constant for the amplitude decay is related with the time constant for the energy decay as $\tau = 2\tau_{eng}$ [49]. This means that the amplitude of the oscillations in the system decays twice as fast as the dissipation of energy.

We can relate the quality factor Q to the complex eigenfrequency of the system $\omega_0 + i/\tau$ via $Q = \omega_0\tau/2$. The time constant for the decay rate is equal to the time necessary for the amplitude to decay by a factor of e^{-1}. The bigger the time constant of the amplitude decay, the lower is the rate at which the energy is dissipated in the system and the higher is the quality factor.

SEM images of the fabricated devices

Dimensions of the fabricated devices were checked using scanning electron microscopy (SEM) with the results presented in Fig. 7. One can see that the achieved periodicity and width of nanostrip resonators hardly deviates from the target values of w_{uc} and w_p.

Optical Constants

The optical constants used in the numerical simulations presented in the article are referenced and plotted below, see Fig. 8. The optical constants for aluminum (Al) are extracted from the work of Rakic *et al.* [57], where the experimental data is fitted using the Brendel-Bormann model. The optical constants for indium tin oxide (ITO) were obtained by ellipsometry measurements. Finally, optical constants of GST are the same as in the work by Ruiz de Galarreta *et al.* [23].

Optics EXPRESS

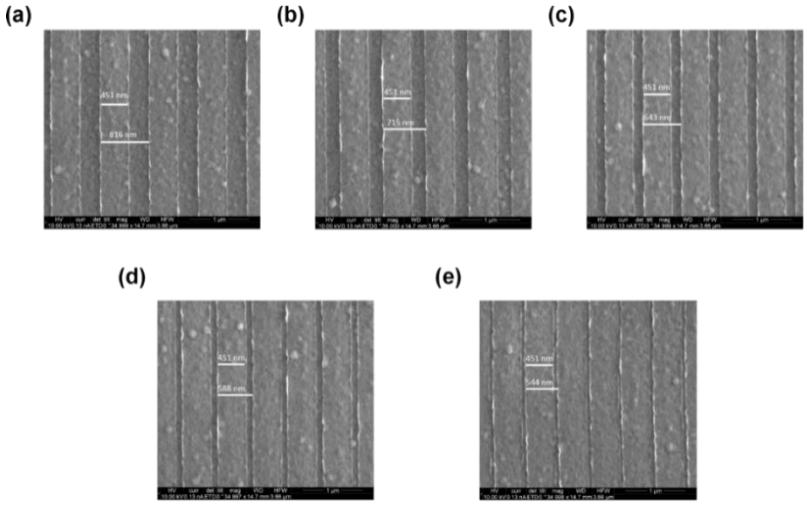

Fig. 7. SEM images of the fabricated phase-change absorber devices. (a) w_{uc} = 816 nm, (b) w_{uc} = 715 nm, (c) w_{uc} = 643 nm, (d) w_{uc} = 588 nm and (e) w_{uc} = 544 nm.

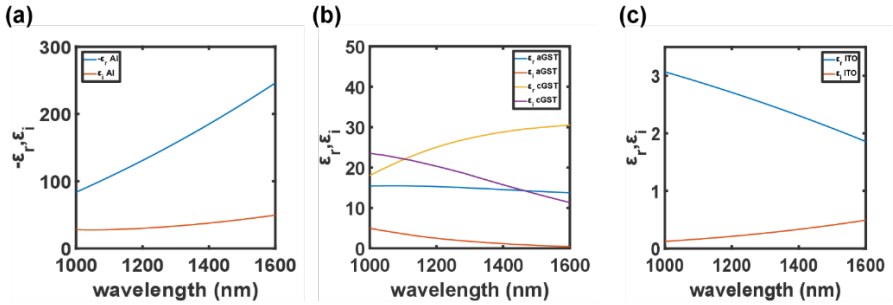

Fig. 8. Optical constants (permittivity) used in numerical simulations. (a) Real and imaginary parts of aluminium permittivity extracted from the work of Rakic *et al.* [57] (b) Real and imaginary part for the GST permittivity in the amorphous and crystalline state from the work by Ruiz de Galarreta *et al.* [23] (c) Real and imaginary part of ITO permittivity obtained by ellipsometry measurements.

Maximum and minimum achievable Q in the structure

The maximum and minimum values for the quality factor fabricated for the structure in the paper (with the restriction of fixed width of the nanostrip and thickness of GST) were found to be Q = 3.55 and Q = 6.26. For values of the quality factor smaller than 3.55 the period in the structures starts to be large enough (>1000 nm) to have higher diffractive orders within the range of measurement. For values of the quality factor bigger than 6.26, the width of the unit cell is close to the width of the nanostrip, making the fabrication of these structures rather difficult. Other kinds of restrictions not arising from the device geometry but due to the optical constants of the materials used may also affect the limits of the range for the achievable Q factors. In particular, the internal losses will be determined by the interaction of the excited resonant fields and the materials that comprise the device. In that case we may expect higher quality factors (lower internal losses) for all-dielectric and hybrid dielectric/plasmonic structures as compared to the purely plasmonic approach presented here.

Phase switching of devices

As discussed in the main text, the switching of phase-change devices requires, for amorphization, temperatures in the phase-change material to reach melting point (~ 900 K for $Ge_2Sb_2Te_5$) and be followed by a very fast cooling (tens of degrees per nanosecond for

Optics EXPRESS

$Ge_2Sb_2Te_5$), while crystallization requires heating to temperatures lying between the glass-transition and melting temperatures. Such heating can be delivered electrically by Joule heating (as is routinely carried out in electrical phase-change memory devices, see. e.g [15], Raoux *et al*.), optically (as in re-writable optical disks, see also [15], Raoux *et al*.) or by using some form of embedded micro-heater (as demonstrated e.g. as in [50], Au *et al*.). In the results below, we demonstrate switching of our absorber type devices using both optical and micro-heater approaches.

Optically induced switching: A 405 nm wavelength (blue) diode laser was scanned across the device to induce reversible switching of absorber devices. The duration and power of the laser pulses was appropriately selected in order of crystallize or re-amorphize the phase-change

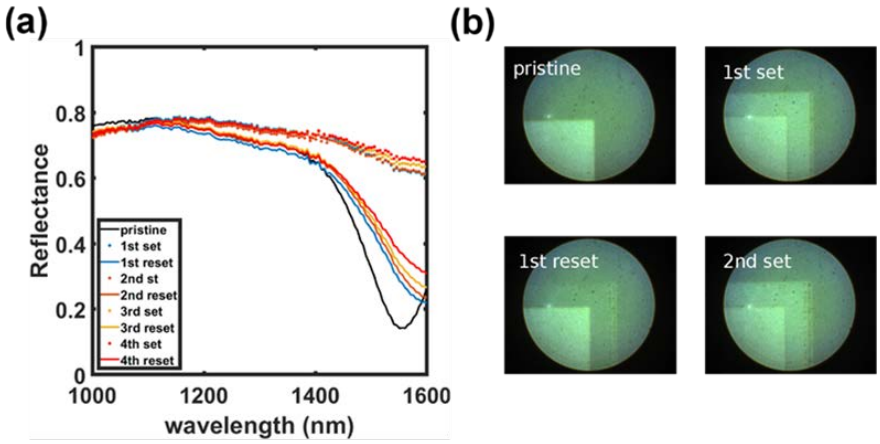

Fig. 9. (a) Reflectance spectra of the absorber device in the pristine (as-deposited) state as well as after several swithing (SET/RESET) cycles. (b) Optical microscope images of the device after a sequence of switching cycles.

layer (specifically crystallization pulses were of 3.6 mW power, at the sample, and 200 ns duration; re-amorphization pulses were of 13 mW power and 15 ns duration). The reflectance spectrum of the device was measured after each crystallization/amorphization (or SET/RESET) process, and the device was also observed in an optical microscope – see Fig. 9. In Fig. 9(a), it can be seen that repeated cycling of the device can be achieved using this laser scanning approach, but that the re-amorphization stage is probably incomplete (since the spectrum for the amorphous phase of the device shifts in wavelength and decreases in absorption with each cycle). Incomplete re-amorphization is not un-expected however when using a scanning laser, since as the laser scans, the periphery of the laser spot can heat previously amorphized regions of the phase-change layer up to a temperature conducive to crystallization (but note that such effects can be reduced/ameliorated by using very large spot sizes, as for example in [16]). Figure 9(b) shows optical microscope images of the device after successive SET/RESET cycles; changes in optical contrast of the phase-change layer are readily seen.

In-situ switching using micro-heater approach: Although optical switching of the phase-change absorber device is possible, it is of course an ex-situ approach (requiring an external laser), and a more attractive approach for practicable devices is some form of in-situ excitation. An already successfully demonstrated in-situ approach is that using a form of micro-heater, as e.g. in [50]. Indeed, for the absorber-type devices, it may well be possible to use the top patterned metal layer as a form of micro-heater, i.e. the metal nanostrips play a dual role, providing both plasmonic effects that drive the optical response and providing heater elements. The basic structure and operation of such an absorber device is shown in Fig. 10: Fig. 10(a) shows the basic concept, Fig. 10(b) an SEM image of an as-fabricated device, and Fig. 10(c)

Optics EXPRESS

shows the reflectance of the device as it is repeatedly switched between amorphous (low reflectance) and crystalline (high reflectance) states.

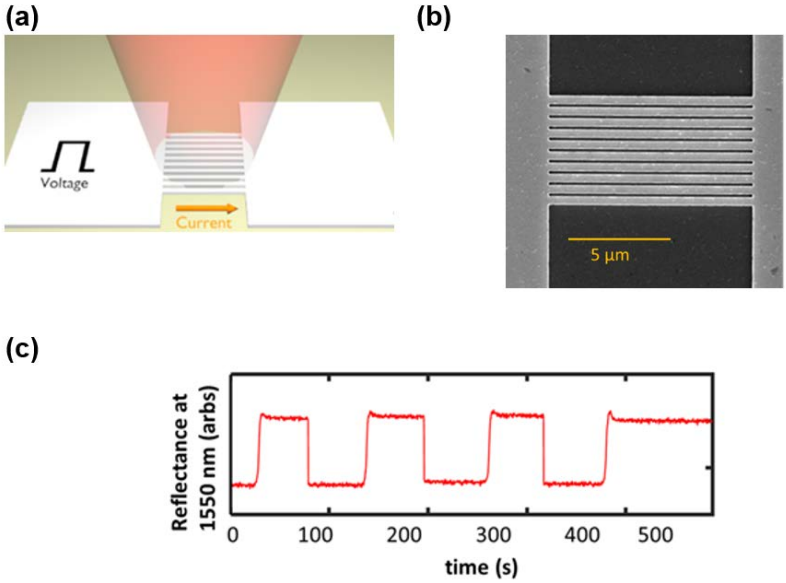

Fig. 10. (a) Schematic of an absorber device in which the top patterned metal layer also acts as a micro-heater to switch the phase-change layer beneath. (b) SEM image of the active area of a fabricated device of the type shown in (a). (c) Measured reflectance of device of the type shown in (b) as it is subjected to repeated cycling (by applying pulsed voltages to the micro-heater).

Funding

US Naval Research Laboratories ONRG programme (#N62909-16-1-2174); EPSRC ChAMP and WAFT grants (EP/M015130/1 and EP/M015173/1; EPSRC CDT in Metamaterials (EP/L015331/1).

Acknowledgments

We thank Dr. Ian R. Hooper of the University of Exeter for interesting discussions on eigenmode calculations. Supporting data for this manuscript is available from the corresponding author.

146.90.84.16 {ts '2018-12-30 15:28:28'}